Journal of Alloys and Compounds 798 (2019) 644–655

Contents lists available at ScienceDirect

Journal of Alloys and Compounds

journal homepage: http://www.elsevier.com/locate/jalcom

Effect of nano-TiB_2 particles on the anisotropy in an AlSi10Mg alloy processed by selective laser melting

Y.K. Xiao [a], Z.Y. Bian [a], Y. Wu [b, **], G. Ji [c], Y.Q. Li [d], M.J. Li [d], Q. Lian [b], Z. Chen [a, *], A. Addad [c], H.W. Wang [a]

[a] State Key Laboratory of Metal Matrix Composites, Shanghai Jiao Tong University, No. 800 Dongchuan Road, Shanghai 200240, China
[b] School of Materials Science & Engineering, Shanghai Jiao Tong University, No. 800 Dongchuan Road, Shanghai 200240, China
[c] Univ. Lille, CNRS, INRA, ENSCL, UMR 8207 - UMET - Unité Matériaux et Transformations, F-59000 Lille, France
[d] Department of Nuclear Physics, China Institute of Atomic Energy, Beijing 102413, China

ARTICLE INFO

Article history:
Received 15 April 2019
Received in revised form
22 May 2019
Accepted 23 May 2019
Available online 28 May 2019

Keywords:
Selective laser melting
In-situ nano-TiB_2 decorated Al alloys
Columnar-to-equiaxed transition
Mechanical properties
Neutron diffraction

ABSTRACT

In components built by selective laser melting (SLM), possible anisotropy in microstructure significantly affects mechanical properties (i.e. service performance) and there is a constant effort to solve this problem. This work carried out a comparative study using fully dense AlSi10Mg alloy and *in-situ* nano-TiB_2 decorated AlSi10Mg composite samples processed by SLM. The aim was at clarifying the effect of integrated nanoparticles on the anisotropy of the as-built component. Microstructure and texture evolution were investigated by scanning and transmission electron microscopy, electron backscatter diffraction, X-ray and neutron diffraction. The SLMed AlSi10Mg sample shows a coarse columnar grain structure with <100> and <110> fiber orientation texture and obvious anisotropy in mechanical properties. However, the nano-TiB_2 modified AlSi10Mg sample exhibits fine equiaxed grains, no preferred crystallographic texture and remarkably reduced anisotropy. Besides, both tensile strength and ductility have been improved in the SLMed TiB_2 decorated AlSi10Mg sample. The preliminary mechanism upon grain refinement effect due to nano-TiB_2 particles on columnar-to-equiaxed transition and reduction of anisotropy was discussed.

1. Introduction

As one of the emerging additive manufacturing (AM) technologies, selective laser melting (SLM) is highly probable to reshape the traditional fabricating industry, particularly in the aerospace and automotive industries demanding for geometrically complex structures [1,2]. The SLM can shorten material development cycle due to the elimination of time-consuming mould design [3], while the rapid solidification (very high cooling rate ~10^5 K/s [4]) involved in the SLM process often conducts to undesirable anisotropic microstructure along the cooling direction (being also parallel to the building direction).

The anisotropy in microstructures and properties has already become a critical issue for the applications of various metallic alloys fabricated by SLM [5–8]. Niendorf et al. [5] have characterized the selective laser melted (SLMed) 316L steel with an extremely high degree of anisotropy featuring coarse elongated grains and a <001> texture alongside the building direction. Simonelli et al. [6] found that the tensile properties and the mechanical anisotropy were affected by crystallographic texture in the SLMed Ti6Al4V alloy. Song et al. [7] observed the columnar microstructure with <100> texture and the anisotropic mechanical behavior in the NiCr alloy parts fabricated by SLM, and found anisotropy weakened with the increase of laser scanning speed. Thijs et al. [8] found that the long columnar grains with <111> preferential crystal orientation along the building direction contribute to yield strength anisotropy in the SLMed Ta alloy.

In general, the origin of the anisotropies in SLMed materials has been ascribed to the formation of coarse columnar grains with preferential crystal orientation along the building direction. Such grains are derived from the high thermal gradients which prevent nucleation ahead of the solidification front, promoting epitaxial grain growth during SLM [8]. Consequently, both the morphological and crystallographic textures contribute to the anisotropy of mechanical properties.

* Corresponding author.
** Corresponding author.
E-mail addresses: eagle51@sjtu.edu.cn (Y. Wu), zhe.chen@sjtu.edu.cn (Z. Chen).

https://doi.org/10.1016/j.jallcom.2019.05.279
0925-8388/

To solve the problem, the mainstream approaches are the optimization of the SLM process parameters and scanning strategy [5,7,9,10]. Nevertheless, they may have negative effects on the densification and mechanical properties of the SLMed samples. Inspired by the grain refinement mechanism in conventional casting processes, the introduction of a grain refiner can effectively remove the columnar grains to achieve the columnar-to-equiaxed transition [11]. Therefore, the introduction of a new nano-structured grain refiner would be an effective way to reduce the anisotropy in the SLM process. As one of the most commonly used grain refiner in Al alloy, TiB_2 particles exhibits good thermal stability and has a well-documented crystallographic orientation relationship with Al [11,12]. In our previous study [13], the *in-situ* nano-TiB_2 decorated AlSi10Mg composite powders (hereafter referred to TiB_2/AlSi10Mg) were used to fabricate composite components by SLM with improved tensile strength and ductility. Nevertheless, the effect of the nano-TiB_2 grain refiner on anisotropic behaviors has not been systematically studied neither in our previous work [14] nor in the references such as in Refs. [15,16]. Likewise, Spierings et al. [17,18] and Li et al. [19] investigated the SLMed Sc-/Zr-modified Al-alloy in which the high content of fine-grained microstructure without any preferential grain orientation was observed. A similar result was obtained in the SLMed AlMgZr alloy with the addition of high content Sc particles, as reported by Kun et al. [20]. Attar et al. [21] and Cai et al. [22] combined in-situ synthetic Ti-TiB2 composites with SLM and explained the strengthening mechanism of TiB2 reinforcements. Martin et al. [23] introduced hydrogen-stabilized zirconium nanoparticles into AA7075 and AA6061 Al alloys resulting in the formation of Al_3Zr nucleant phase, thus to achieve the high-strength Al alloys with crack-free, equiaxed, fine-grained microstructures.

In this paper, the TiB_2/AlSi10Mg powders were used as a model system to study the effect of the nanosized grain refiner particles on the reduction of anisotropy during SLM. The powders were synthesized via the salt-melted reaction followed by gas-atomization [14,24]. Microstructural characterization and mechanical properties of the SLMed AlSi10Mg alloy and TiB_2/AlSi10Mg composite components are systematically studied and compared to better understand the underlying mechanism. This work highlights the importance of design and fabrication of suitable grain refiner decorated powders to solve the anisotropy problem in SLMed components.

Table 1
Chemical composition of AlSi10Mg and TiB_2 decorated AlSi10Mg powders (wt. %).

Element	Si	Mg	Cu	Mn	Ti	B	Al
AlSi10Mg alloy	10.0	0.3220	0.0278	0.0011	–	–	Balance
TiB_2/AlSi10Mg	9.81	0.3226	0.0241	0.0085	3.842	1.761	Balance

2. Materials and experimental procedures

2.1. Materials

The powder material of the nano-TiB_2 decorated AlSi10Mg alloy (i.e., TiB_2/AlSi10Mg alloy) was fabricated by the in-situ salt-metal reaction method as described in Refs. [13,24]. The powder was produced by gas atomization using the high-purity inert He gas atmosphere to minimize oxidation [14]. The TiB_2 particles have a wide size distribution in the matrix and most are less than 100 nm according to our previous study [25].

The AlSi10Mg alloy powder supplied by VILORY Ltd, Jiangsu, China was used for comparison. Chemical composition of the AlSi10Mg and TiB_2/AlSi10Mg alloy powders were determined using ICP-AES (Inductively Couple Plasma Atomic Emission Spectroscopy, iCAP6300), as listed in Table 1. Fig. 1 shows the SEM images of AlSi10Mg and TiB_2/AlSi10Mg alloy powders, which mostly have a spherical shape. The diameter ranges of both powder samples are 15–53 μm. The volume fraction of TiB_2 is 3.4 vol%, corresponding to 5.6 wt% weight fraction of Ti and B element in Table 1.

2.2. SLM process

The experiments were carried out at room temperature on a Prox DMP 200 SLM machine (3D Systems, USA), with a maximum laser output power of 300 W, a wavelength of 1070 nm and a focused laser beam spot diameter of 75 μm. Based on a series of preliminary experiments, the optimum processing parameters at which the highest relative density was achieved, were listed in Table 2. The porosity analysis was checked to be 99.971% for AlSi10Mg alloy and 99.975% for TiB_2/AlSi10Mg sample, using computed tomography (CT, Metrotom 800, ZEISS). Layers with a thickness of 30 μm were used with a hatching space of 100 μm and a scanning strategy of rotation for 90°between layers. The whole

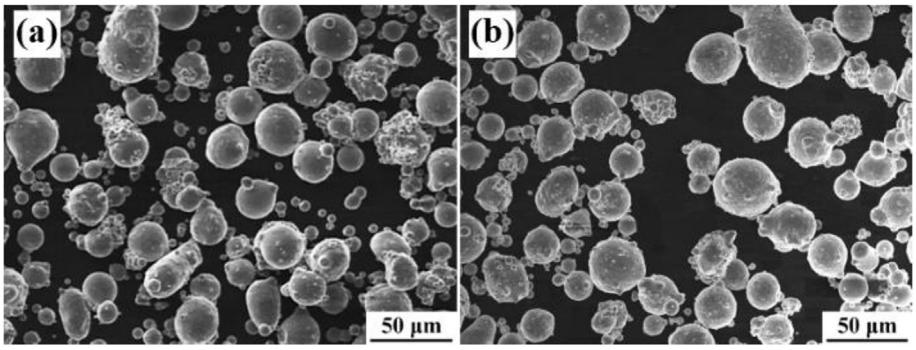

Fig. 1. SEM images of powder morphology: (a) AlSi10Mg and (b) TiB_2/AlSi10Mg alloys.

Table 2
Optimum process parameters used for AlSi10Mg and TiB_2 decorated AlSi10Mg alloys.

Optimum Parameters	Laser power, W	Scanning speed, mm/s	Layer thickness, μm	Hatching space, μm
AlSi10Mg alloy	200	1200	30	100
TiB_2/AlSi10Mg	210	1000	30	100

process was carried out in a high purity Argon atmosphere flow with an oxygen-content <500 ppm to minimize in-situ oxygen pick-up.

As can be seen from Fig. 2a, the cylindrical samples were built along the building direction (z-direction) and perpendicular to the z-direction. The samples were machined to tensile bars. As-built samples were cut along the XY and XZ planes for top- and side-view cross-sections for microstructure characterization, respectively.

2.3. Microstructure characterization

Specimens were prepared using the standard metallographic techniques and etched with Keller's reagent (the aqueous solution of 2.5 vol% HNO_3, 1.5 vol% HCl, 1 vol% HF) for 1 min. The electron backscatter diffraction (EBSD) samples were grinded and then ion polished on the Leica EM TIC 3X machine. The microstructural morphology of the powders and SLMed samples were examined by scanning electron microscopy (SEM, TESCAN MAIA3). The microscopic texture, crystallography and grain size of the samples were investigated using EBSD with a step size of 0.172 μm, which was characterized on a TESCAN MAIA3 SEM equipped with a BRUKER e-Flash^{HR} EBSD detector and the energy dispersive X-ray spectroscopy (EDX, Oxford Instruments) system. Then, the EBSD Kikuchi patterns were post-treated by CHANNEL 5.0 software package. TEM thin foils of the SLMed samples were prepared by mechanically polishing and finally ion thinning on a Precision Ion Polishing System (Gatan Model 691) and examined using an FEI Talos F200X transmission electron microscope operating at 200 kV.

Phase determination of the powders and SLMed samples was done by X-ray diffraction (XRD, Ultima IV X-ray diffractometer) with Cu Kα radiation (λ = 0.1542 nm) setting in the 2θ range from 20° to 50° and scanning speed of 5°/min.

2.4. Neutron diffraction

Neutron diffraction is a very suitable and effective tool for measuring the bulk microstructure of engineering materials owing to the deep penetration of neutrons. The texture of SLMed cube shaped samples ($10 \times 10 \times 10$ mm^3) were analyzed in transmission mode at neutron diffractometer, laboratory CARR, China Institute of Atomic Energy, Beijing, China using a wavelength of 0.148 nm. The tilt angle χ changes from 0° to 90° and the azimuth angle φ varies from 0° to 360° with a step of 5°.

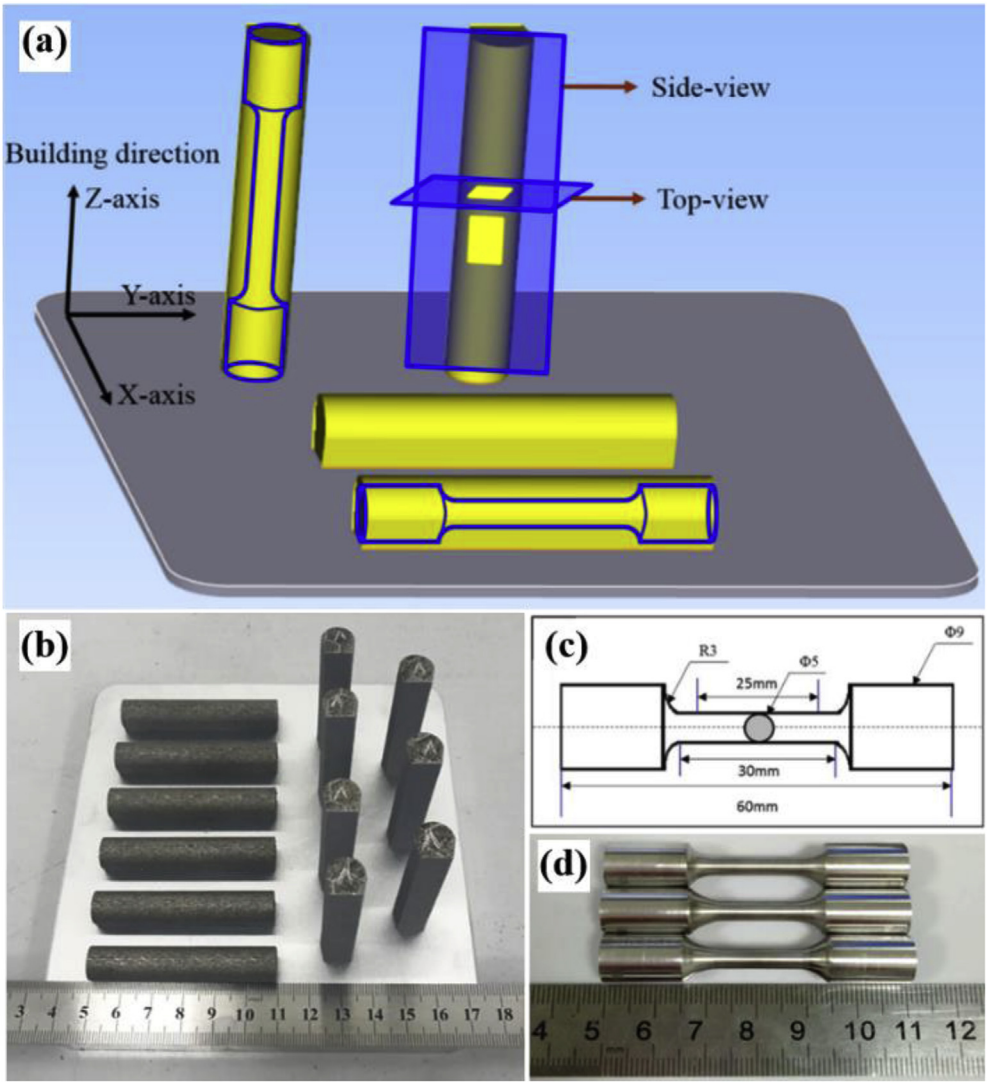

Fig. 2. SLMed specimens: (a) Schematic diagram (b) Room temperature tensile parts at two directions, (c) configuration (Gage length: 25 mm), and (d) tensile specimens after machining.

2.5. Mechanical properties

Fig. 2b illustrates the samples built vertically and horizontally according to Fig. 2a. The dog-bone tensile testing specimens in Fig. 2d were machined according to the ASTM-E8M standard, as the configuration shown in Fig. 2c. The tests were carried out on a Zwick/Roell Z100 testing machine at a constant strain rate of 10^{-4} s^{-1} and the strain was measured with a 10 mm gauge length extensometer.

2.6. Measurement of thermal conductivity

Thermal conductivities of the SLMed AlSi10Mg and TiB_2/AlSi10Mg samples were measured in the temperature range 20–500 °C using a Laserflash apparatus (LFA 467, Netzsch). The experimental samples were in the square sheet (10 × 10 mm) with a thickness of 2 mm and mechanically polished.

3. Results

3.1. Microstructure

3.1.1. Microstructure characterization by SEM

The SEM images in the vertical direction (Side-view in Fig. 2a) of SLMed AlSi10Mg and *in-situ* TiB_2 decorated AlSi10Mg samples are shown in Fig. 3 to investigate the typical microstructure. Fig. 3a shows the morphology of columnar cells in AlSi10Mg alloy. The grey area is α-Al cells. The brighter eutectic Si meshes are in the rod-like shape and the strips are elongated in the building direction. The aspect ratio of elongated cellular sub-structure is up to 4–5. As reported earlier, the columnar grains contain a cell-like sub-structure elongated in the building direction [26,27], which is also observed in this study.

Fig. 3b shows the microstructure of the SLMed TiB_2/AlSi10Mg alloy, which shows similar α-Al cells separated by Si boundaries. But the cells are uniformly ultrafine equiaxed and there is no obvious directionality. A few TiB_2 particles aggregated at the common vertex of multiple cells can be recognized. Consequently, with the introduction of nano-TiB_2 particles, the microstructure of the elongated dendritic cells has been refined and the columnar structure has been eliminated.

In order to show the distribution of TiB_2 particles, over etching TiB_2/AlSi10Mg samples are prepared and the microstructure is shown in Fig. 3c. The TiB_2 particles are mainly dispersed along the cell boundaries (CBs) with some aggregation at the common vertex of multiple cells. Besides, a large number of nanostructured TiB_2 particles can be observed in the sample. The higher magnification image shows that the TiB_2 particles with a size of <500 nm exhibited cubic prism-like morphology with clear edges and corners.

3.1.2. Grain structure evolution

The EBSD inverse pole figures (IPF) of longitudinal-section along the building direction (Side-view) and cross-section perpendicular to the building direction (Top-view) of both SLMed samples are shown in Fig. 4. The side-view of SLMed AlSi10Mg alloy in Fig. 4a shows the elongated grain structure of the commonly reported melt pools [20,27,28], and the boundaries of melt pools are shown in the figure marked with black dashed lines. Small equiaxed grains (<2 μm) are observed at the edge of the melt pool with random orientations. But the coarse columnar grains (>10 μm) cover most of the area (74.4%) by EBSD grain area analysis. Fig. 4b is the higher magnification of the box area in Fig. 4a with lots of small grains at the edge of the melt pool. Such a fine microstructure can be ascribed to the high cooling rate during the SLM process and the nucleation effect of already solidified grains [29]. It can be still observed that obvious large columnar grains (~20 μm in length) intertwined with and roughly along the building direction. Fig. 4c gives the top-view of SLMed AlSi10Mg alloy, revealing the cross-section of coarse elongated grains.

In contrast, the side-view and top-view of SLMed TiB_2 decorated AlSi10Mg alloy in Fig. 4d and e show the fine equiaxed grain microstructure with a diameter of about 2 μm in both longitudinal and cross section. Besides, the commonly reported melt pool structure cannot be observed. Simultaneously, it is clear to observe the uniform distribution of TiB_2 particle (black dots in Fig. 4d and e, some indicated by short black arrows) throughout the sample. Most of the particles are distributed along the grain boundaries, while some of the particles within the equiaxed grain.

Fig. 4f shows the grain size distributions of the SLMed AlSi10Mg and TiB_2/AlSi10Mg components. According to the grain size distribution statistics, none ultrafine grains (grain size <1 μm) are present in the alloy component without TiB_2 particles. As listed in Table 3, the average grain size of the alloy is around 4.48 μm in the side view with 75% of area fraction composed of grains larger than 10 μm. Comparatively, the 43.1% of the grains in the SLMed TiB_2/AlSi10Mg sample are less than 1 μm; the average grain size is reduced by more than 50% to around 2.08 μm, and the grains larger than 10 μm only accounts for 5.6%. Fig. 4g gives the histogram of the aspect ratio (AR) in the function of grain size. It can be clearly found that the AR of the columnar grains increases with the grain size of the AlSi10Mg alloy. Combining with Table 3, the average AR is 4.27 in the side view indicating that the coarse columnar grains dominate the microstructure of the AlSi10Mg alloy. While the AR

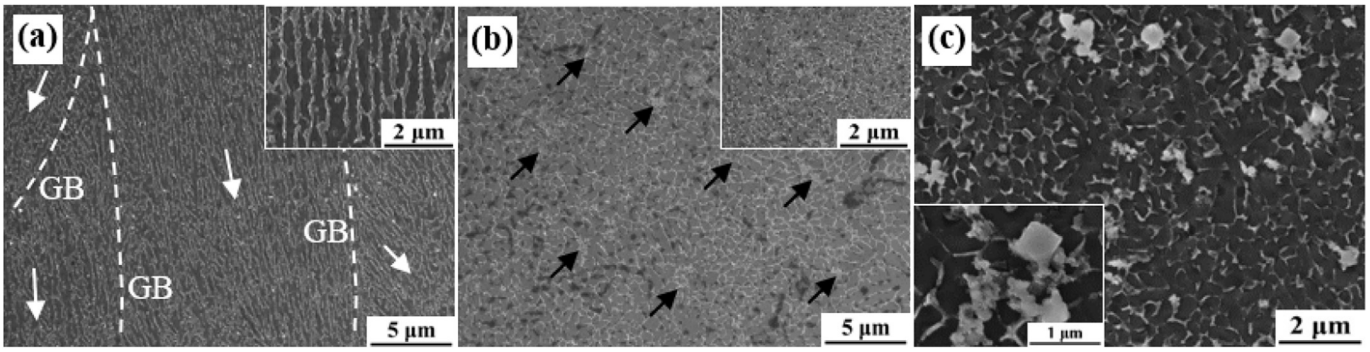

Fig. 3. SEM images of SLMed samples in vertical direction (Side-view): (a) AlSi10Mg alloy; (b) TiB_2/AlSi10Mg alloy; (c) Over etched TiB_2/AlSi10Mg alloy. Inset in each figure is in a higher magnification. White dashed lines in (a) point to grain boundaries (GB) and the white arrows point to the direction of cells elongation. Black arrows in (b) point to TiB_2 particles.

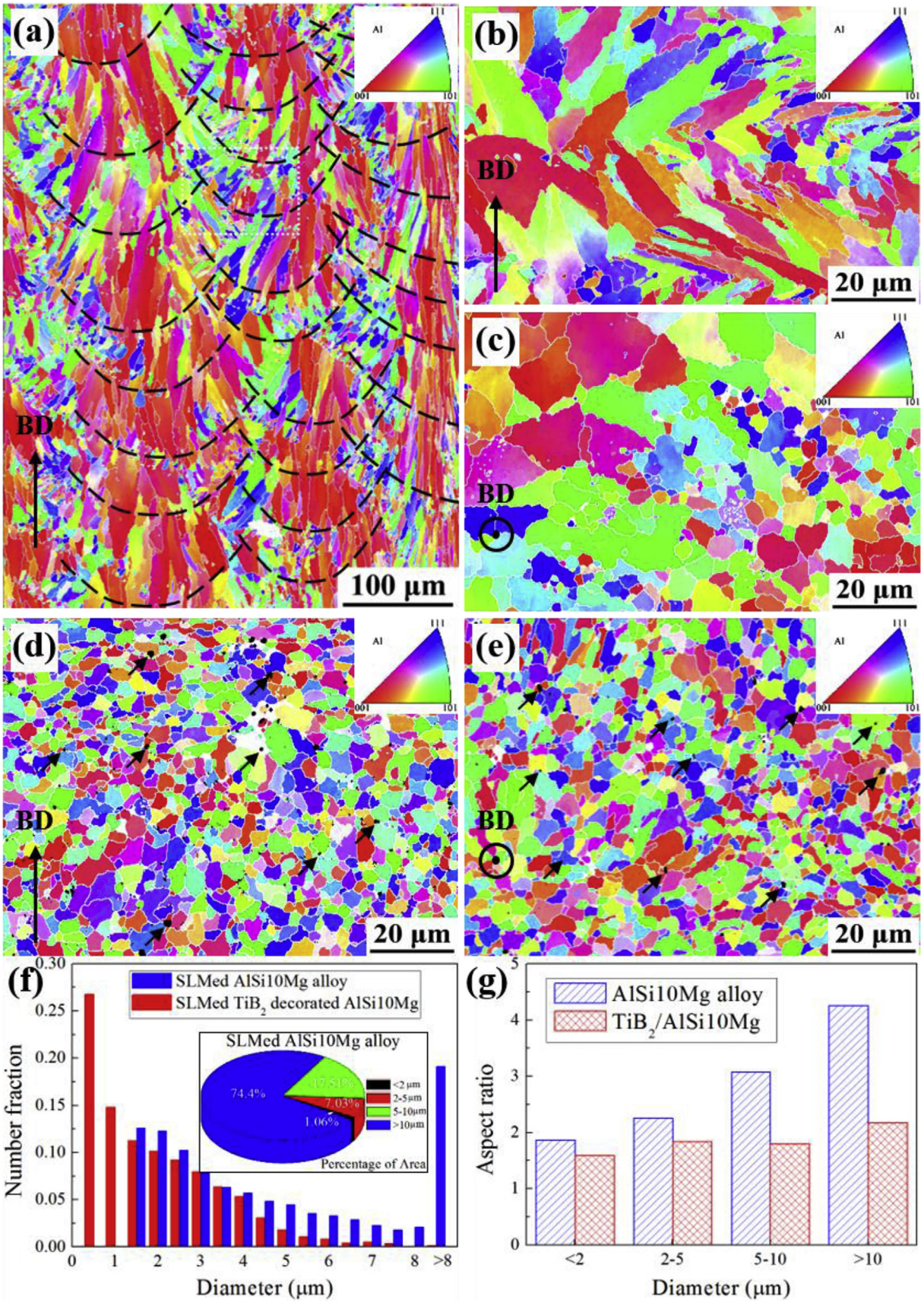

Fig. 4. EBSD inverse pole figure (IPF) maps in two perpendicular views of SLMed AlSi10Mg and TiB_2/AlSi10Mg alloy: (a) side-view, (b) side-view in a higher magnification in the box area in (a) and (c) top-view of the AlSi10Mg alloy; (d) side-view and (e) top view of the TiB_2/AlSi10Mg composite. Black dashed lines in (a) indicate melting pool boundaries, the long black arrows on the pictures indicate the building direction and the short black arrows in (d, e) point to TiB_2 particles. (f) Grain size distribution statistics of SLMed AlSi10Mg and TiB_2 decorated AlSi10Mg alloy, inset is the area percentage pie chart of different grain sizes of SLMed AlSi10Mg alloy; (g) The histogram of the aspect ratio as a function of grain size for the two samples.

Table 3
The diameter and aspect ratio of grains in different directions of SLMed samples.

Sample	Surface	Diameter (μm)	Average diameter (μm)	Area percentage of grains >10 μm (%)	Aspect ratio
AlSi10Mg alloy	top	4.80	4.48	74.4	1.85
	side	4.15			4.27
TiB_2/AlSi10Mg	top	1.76	2.08	5.6	1.85
	side	2.41			1.84

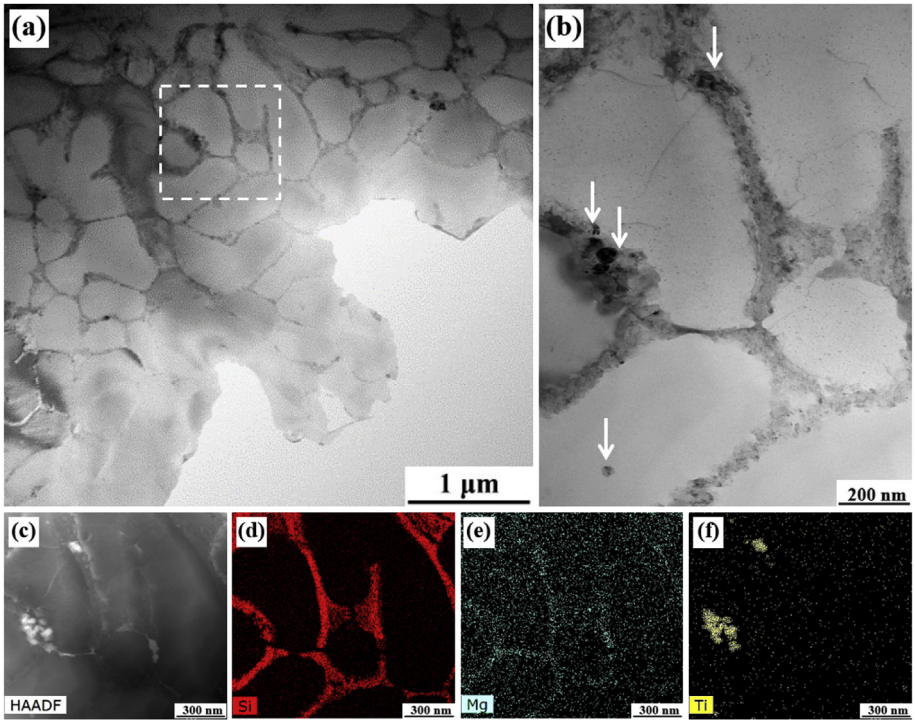

Fig. 5. (a) TEM BF images of the SLMed TiB_2/AlSi10Mg composite sample, (b) zoom-in image of the box area shown in (a), (c–f) STEM HAADF image and corresponding EDX maps of Si, Mg and Ti elements.

significantly reduces to 1.84 and remains almost unchanged in the SLMed TiB_2/AlSi10Mg composite. As such, the fine equiaxed grains are the preferred solidification structure in TiB_2/AlSi10Mg sample.

3.1.3. Sub-structure observation by TEM

The typical bright field (BF) TEM images of the microstructure of the SLMed TiB_2 decorated AlSi10Mg sample are shown in Fig. 5a and the fine cell structures with a size of 500 nm to 1 μm can be observed. From the higher magnification in Fig. 5b, nano-TiB_2 particles are distributed mainly along the cell boundaries and a few inside the cell. The STEM HADDF image and corresponding EDX mappings of the TiB_2 decorated AlSi10Mg alloy are shown in Fig. 5c–f. It can be clearly seen that Si and Mg accumulate along the cell boundary, and some Ti distributes along the boundary which is consistent with BF results.

3.2. Texture evolution

3.2.1. Preliminary analysis by XRD

Fig. 6 exhibits the XRD patterns of SLMed AlSi10Mg and TiB_2 decorated AlSi10Mg samples. It can be seen that every pattern exhibits peaks corresponding to the face-centered cubic (FCC) α-Al and the diamond-like cubic Si phase, while the hexagonal TiB_2 phase only appears in the TiB_2 decorated AlSi10Mg material. It must be mentioned that the relative intensity of the α-Al (200) peak ($I_{(200)}$) is much higher than that in the reference (PDF reference pattern: 04-0787) and even stronger than $I_{(111)}$ in SLMed AlSi10Mg alloy. The ratio of (200) peak to (111) peak in SLMed AlSi10Mg alloy is 1.21 much larger than the ratio in the reference (0.47). The result suggests that the crystal face (200) is the preferred orientation of α-Al crystal in the SLMed AlSi10Mg alloy. The favorable <100> fiber texture is similar to that observed for other SLMed Al-based alloy in works of literature, such as Al-12Si alloy [30] and AlZnMgCu alloy [31].

However, in SLMed TiB_2 decorated AlSi10Mg alloy, the relative intensity of the α-Al (200) peak is dramatically weakened. The intensity of diffraction peaks is almost the same with the reference. Besides, the ratio of (200) peak to (111) peak in SLMed TiB_2 decorated AlSi10Mg alloy is 0.41, which is very close to the value of the non-textured reference.

3.2.2. Microtexture from EBSD

The {100} pole figures (from EBSD data) of the SLMed AlSi10Mg and TiB_2 decorated AlSi10Mg alloy are shown in Fig. 7a and b. Although there is a slight misalignment, the strong <100> texture exists along the building direction and the highest intensity is 9.81 in SLMed AlSi10Mg alloy. Combined with the front IPF result, it indicates that the majority of columnar grains have their preferred <100> orientation parallel to the building direction. The apparent fiber texture around the centerline might be due to the existence of

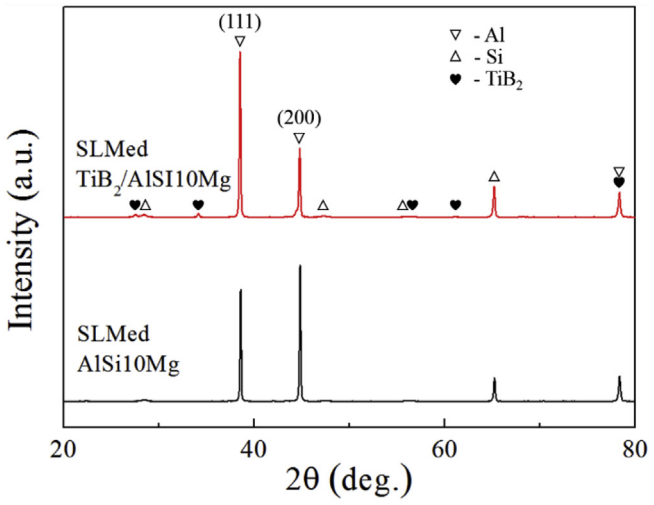

Fig. 6. XRD patterns of SLMed AlSi10Mg and TiB_2 decorated AlSi10Mg samples.

a high thermal gradient along the building direction. In contrast, in the SLMed TiB_2 decorated AlSi10Mg alloy, almost none texture can be observed and the maximum intensity is only 1.47 in the pole figure.

The grain boundary misorientation distributions (averaged over several EBSD maps for each sample) for the SLMed AlSi10Mg and TiB_2 decorated AlSi10Mg alloy are shown in Fig. 7c and d, respectively. It is clear that the HAGB fraction of the TiB_2 decorated AlSi10Mg alloy accounts for 98.0%, which is apparently higher than the value of the AlSi10Mg base alloy (84.6%). This means some new high misorientation boundaries are produced owing to the heterogeneous nucleation effect of nano-TiB_2 particles. The distribution of misorientation angles of TiB_2/AlSi10Mg sample is in accordance with a randomly texture ideal polycrystalline material.

3.2.3. Bulk texture analysis by neutron diffraction

The bulk texture analysis of the SLMed AlSi10Mg and TiB_2 decorated AlSi10Mg alloy investigated by neutron diffraction is shown in Fig. 8. The {100} pole figure parallel to the BD and three-dimensional orientation distribution functions (3D ODF) of AlSi10Mg alloy are shown in Fig. 8a and c. As previously mentioned, the typical texture of SLMed AlSi10Mg alloy is defined as <100> fiber texture parallel to the BD. The maximum intensity could reach 2.39 in the pole figure. Unexpectedly, the weak <110> fiber texture is discovered in SLMed Al alloy. The overall crystallographic texture sharpness index calculated from the orientation distribution function *f(g)* is defined by Ref. [32]:

$$\text{Texture Index} = I_{tex} = \int_{eulerspace} (f(g))^2 dg \quad (1)$$

where *f* if the orientation distribution function; *g* is the Euler space coordinates.

The texture index (I_{tex}) of AlSi10Mg alloy was 1.21 by calculation. This is in good consistent with the value (texture index 1.266) in literature [27]. The texture index equals to unity for isotropic material [32]. Furthermore, the volume fractions (f_{vol}) of the <100> and <110> fibers are calculated here by the integration of the ODF intensities considering a 10°, 15° and 20° misorientation from the center position of the ideal fiber orientation. The corresponding fiber volume fractions with the above divergent angle for the two samples are shown in Fig. 8d. These results show that the <100> fiber and <110> fiber textures of the SLMed AlSi10Mg alloy are not very sharp, however, the majority of the grains (approximately 60% in volume fraction) are oriented around the two directions.

When the nano-TiB_2 particles are introduced, the overall crystallographic texture is significantly reduced, as shown in the {100} pole figure in Fig. 8b. The neutron diffraction result shows the weak texture with a maximum density near to 1.18. The calculated

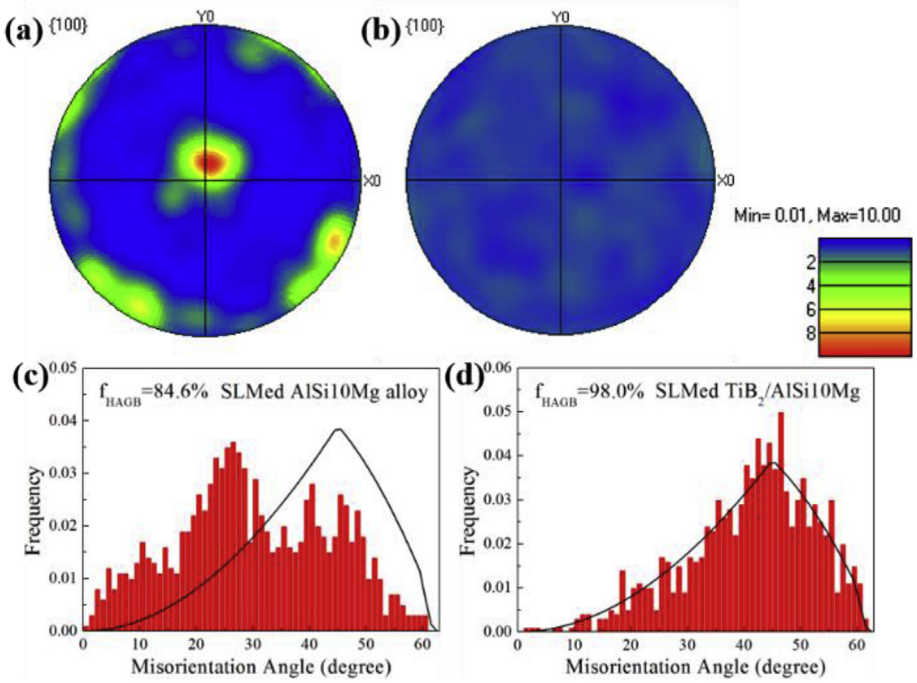

Fig. 7. Pole figures of the side view for SLMed samples: (a) AlSi10Mg alloy along the center line of the melt pool in Fig. 4(a) (factor 9.81); (b) TiB_2 decorated AlSi10Mg alloy corresponding Fig. 4(d) (factor 1.47). Grain boundary misorientation distributions for (c) SLMed AlSi10Mg alloy; (d) SLMed TiB_2 decorated AlSi10Mg alloy, solid lines show the random Mackenzie distribution.

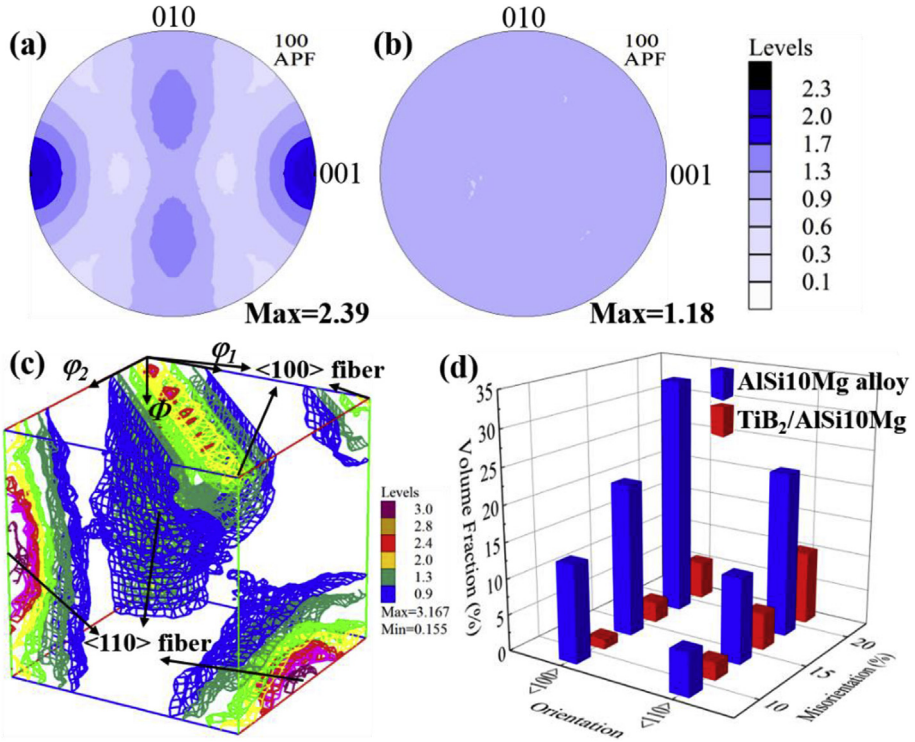

Fig. 8. The {100} pole figures of SLMed (a) AlSi10Mg and (b) TiB_2 decorated AlSi10Mg alloy. (c) 3D ODF for SLMed AlSi10Mg alloy; (d) volume fraction of texture components in the two SLMed alloys.

texture index is lowered to 1.09 and the volume fraction of both <100> and <110> orientation is close to the value for ideal isotropic material. In addition, it is remarkable that the corresponding fiber volume fractions are decreasing significantly for the existence of nano-TiB_2 particles. By comparing the above results, we found that the strong <100> fiber texture along the building direction and sub-strong <110> fiber texture has developed into a particularly randomized texture.

3.3. Mechanical properties

The tensile testing of SLMed AlSi10Mg alloy and TiB_2 decorated AlSi10Mg samples in the different directions were performed. Fig. 9a displays the typical stress-strain curves for each material; the associated ultimate tensile strength (UTS) and elongation to failure (El) are summarized in Table 4. In detail, the UTS in the vertical direction (//BD) of AlSi10Mg alloy is 487.27 ± 3.41 MPa and El is 3.90 ± 0.03%, while in the horizontal direction the UTS is 437.54 ± 1.60 MPa and El is 2.94 ± 0.44%. The difference of UTS in two directions is 12.14% (53 MPa) and El is 32.65%. In comparison, the differences of that in TiB_2 decorated AlSi10Mg alloy significantly decrease to 1.26% (7 MPa) and 15.27%. Additionally, the strength and ductility have been dramatically improved simultaneously in the SLMed AlSi10Mg alloy with the incorporation of TiB_2 nucleant particles.

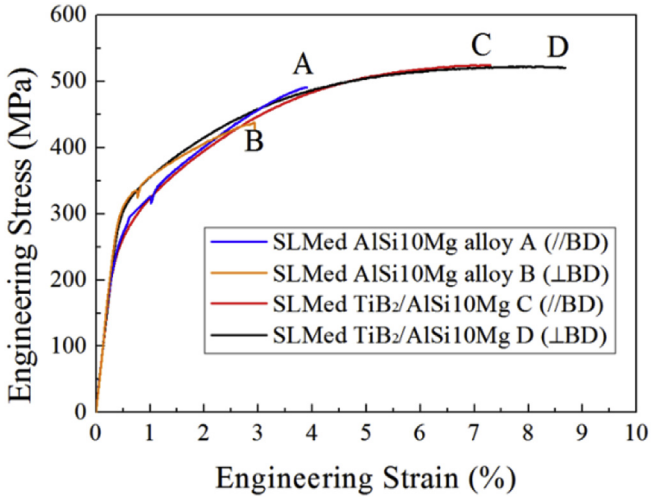

Fig. 9. The tensile stress-strain curves of the SLMed AlSi10Mg and TiB_2 decorated AlSi10Mg alloy.

Table 4
Tensile properties of the SLMed samples in two directions.

Sample	Direction	UTS (MPa)	Difference in UTS (%)	El (%)	Difference in El (%)
AlSi10Mg alloy	//BD	490.64 ± 3.41	12.14	3.90 ± 0.03	32.65
	⊥BD	437.54 ± 1.60		2.94 ± 0.44	
TiB_2/AlSi10Mg	//BD	529.60 ± 4.58	1.26	7.53 ± 0.15	15.27
	⊥BD	522.91 ± 3.59		8.68 ± 0.49	

4. Discussion

4.1. The effects of nano-TiB_2 particles on the microstructure and texture

For the high heating and cooling rate (10^3–10^5 K/s) during SLM process, the solidification microstructures obtained through SLM are expected to be complex, especially the hierarchical structure of grains and cells in SLM Al-Si alloys [13,33]. In our previous study [13], we focused on the formation mechanism of non-equilibrium supersaturated Al cells, eutectic Al-Si at the cell boundaries related to the nano-TiB_2 and the freeze-in effect for the high cooling rate. In this paper, we will concentrate on the grain structure and texture evolution during the rapid solidification process. During the brief interaction between laser and powder, the powder material is melted and thus forming the extremely small melt pool dimensions of several tens of micrometers to hundreds of micrometers [2,34]. Subsequently, a large number of fine equiaxed grains are nucleated at the edge of the melt pool. As a result of directional heat flux and thermal gradient intrinsically associated with the SLM process, coarse grains are nucleated by those underlying fine grains. During this stage, the directional solidification along the thermal gradient results in columnar grains with the most favorable growth direction [28,35]. Moreover, the previously solidified layer should be remelted again when the next layer is scanned and the remelting thickness is ~30 μm equal to the height of melt pool (~60 μm from Fig. 4) subtracting the layer thickness (30 μm). Finally, the coarse columnar grains grow epitaxially from the remelted layer along the building direction. As for the crystallographic relationships in the SLMed FCC Al-based alloys, it has been shown that the coarse columnar grains not only grow along the usual <100> crystallographic direction, but also lie along a <110> direction. The new observation of <110> dendrite growth direction in SLMed Al alloy can't be explained by the commonly accepted theory of steady-state dendrite growth. The similar dendrite growth direction of <110> was also observed for high thermal gradient and cooling rate during cast by Henry et al. [36,37] and Haxhimali et al. [38]. The competition of columnar grains growth direction between <100> and <110> can be attributed to the high solidification rate in the melting pool and/or the modification of solid-liquid interfacial energy and/or attachment kinetics anisotropy caused by solute elements. Further research is carrying out to reveal the underlying mechanism of the <100> and <110> texture formation during the unique condition of SLM.

In the nano-TiB_2 decorated AlSi10Mg alloy, the nano-TiB_2 particles play a key role in grain refinement and formation of equiaxed grains. As known, TiB_2 is the most widely used grain refiner for Al alloys. The nano-TiB_2 particles should act as effective seed crystals for Al-matrix grain growth due to the well documented crystallographic orientation relationships (ORs) [13,14], i.e. $(0001)_{TiB2}//(-111)_{Al}$, $[11\bar{2}0]_{TiB2}//[110]_{Al}$ and $(1\text{-}101)_{TiB2}//(001)_{Al}$, $[11\bar{2}0]_{TiB2}//[110]_{Al}$. At the first stage of solidification during SLM, nano-TiB_2 particles serve as nuclei for α-Al grains. The high resolution TEM (HRTEM) image and corresponding fast Fourier transform (FFT) patterns of the interface between the nano-TiB_2 and Al are shown in Fig. 10. The parallel lattice fringes of the two sets of planes can be clearly seen at the interface between Al and TiB_2 in Fig. 10a. The FFT patterns recorded from the Al matrix and Al/TiB_2 interface in Fig. 10b and d, and the corresponding simulated zone-axis diffraction patterns in Fig. 10c and e show the highly coherent crystallographic orientation relationships. Nano-TiB_2 particles provide a high density of potent nucleation sites in the melt, accordingly, the presence of a large number of low energy barrier nucleation sites reduces the critical amount of total undercooling required to induce equiaxed crystal growth. The presence of nano-TiB_2 nucleant particles indeed plays a critical role in the columnar-to-equiaxed transition. Moreover, it should be pointed out that the nano-TiB_2 particles have good stability in the melt pool due to its high melting temperature ~3230 °C. Therefore, these refractory nano-TiB_2 particles can exist anywhere in the melt pool and serve as inoculants for the nucleation of fine microstructures.

It is particularly worth mentioning that the random orientation of nano-TiB_2 nucleation agents in the melt pool determines the random orientation of Al grains and eutectic Si phase. As a result, the nano-TiB_2 nucleant particles play an important role in the columnar-to-equiaxed transition, which is consistent with the completely fine equiaxed grains from our previous EBSD results.

Subsequently, the nano-TiB_2 particles act as growth inhibitor like pins during the solidification process. The refractory nano-TiB_2 particles prevent the movement of high- and low-angle grain boundaries, hence constraining the growth of grains along the heat flux direction. Such grain boundary pinning effect helps to stabilize against grain growth during the heat impact for melting the subsequent layers. To sum up, the nano-TiB_2 particles in high number densities act as inoculants for Al grains but also, pin and stabilize grain boundaries. Consequently, a very fine-grained microstructure without any texture can be observed in the nano-TiB_2 particles decorated AlSi10Mg alloy.

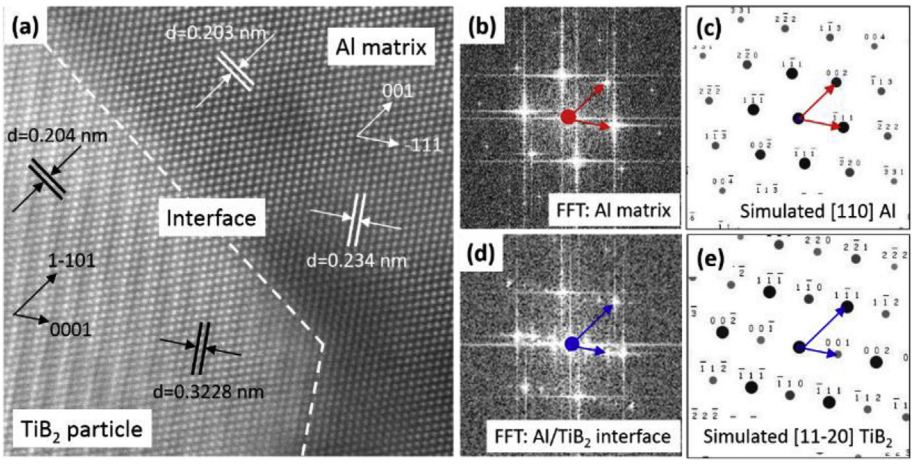

Fig. 10. (a) HRTEM image showing the Al/TiB_2 interface area, (b) and (d) FFT patterns recorded from the Al matrix and Al/TiB_2 interface and (c) and (e) simulated [110] Al and [11–20] TiB_2 zone-axis diffraction patterns corresponding to (b) and (d), respectively.

4.2. The effects of nano-TiB_2 particles on the thermokinetics of SLM

In the SLM forming process, the laser beam with high-energy irradiates on the powders and forms a melting pool. During the solidification of the melting pool, there is an instantaneous thermal gradient from the boundary to the center in the molten pool. It is worth noting that, for the current heat sources of the molten pool, there is argon atmosphere with extremely low thermal conductivity (0.018 W/(m·K)), loose powder and argon around the horizontal direction, and SLMed metal components with high heat conductivity (100–200 W/(m·K)) downward. Hence, a persistent temperature gradient is always existing from the top pool through the already solidified component to the bottom of the building platform during the whole SLM process.

Based on the theory of solidification, it is universally known that low G/R (ratio of thermal gradient to solidification rate) is propitious to the formation of equiaxed grains [39]. However, the maximum temperature gradient (G) can even reach 10^7 K/m during SLM from the simulation results [40], which can give rise to large G/R and hence cell microstructure and columnar grains in SLM processing. The most significant parameter during SLM process is an important combinational parameter called the volumetric energy density (E_v, J/mm^3). It corresponds to the averaged energy provided by the laser beam to the volumetric unit of powders and is defined by Ref. [41]:

$$E_v = \frac{P}{v \cdot t \cdot h}$$

where P is the laser power; v is the laser scanning speed; t is the layer thickness; h is the hatching space.

After summarizing the results of literature [5,7,42], we can conclude that the maximum temperature gradient within the molten pool increases significantly with the increase of the applied E_v. According to the optimum process parameters in Table 2, the energy density of SLMed composite ($E_{v\ \text{of composite}} = 66.67$ J/mm^3) is 20% larger than that of SLMed alloy ($E_{v\ \text{of alloy}} = 55.56$ J/mm^3). Therefore, the anisotropy in microstructure and mechanical property should be more apparent in SLMed nano-TiB_2 modified AlSi10Mg alloy. However, the result shows that the fiber texture is eliminated and properties present isotropy. As discussed above, the prime reason for the formation of ultrafine equiaxed microstructure and crystals is the presence of TiB_2 nucleant particles during SLM. The presence of TiB_2 particles affects the heat transfer in solidification. As we know, the thermal conductivity of the TiB_2 ceramic particles is much lower than the Al matrix. The quantitative thermal conductivity result of SLMed AlSi10Mg alloy and TiB_2/AlSi10Mg sample is shown in Fig. 11. The TiB_2 particles reduce the thermal conductivity of AlSi10Mg alloy by nearly 10% at room temperature. Moreover, the effect of TiB_2 on thermal conductivity decreasing is more and more remarkable with the increase of temperature. It can be reasonably expected that TiB_2 particles should hinder the heat flux more greatly at high temperature so that the heat would accumulate in the material. This effect weakens the gradient of temperature, thus forms fined equiaxed grains and weakens the texture and anisotropy in SLMed AlSi10Mg alloy.

4.3. The effects of nano-TiB_2 particles on the mechanical behavior

The SLMed TiB_2 decorated AlSi10Mg alloy shows an ultimate tensile strength of ~530 MPa. The increment in strength is more than 60 MPa in contrast with SLMed AlSi10Mg alloy without nano-TiB_2. The ductility has also been greatly improved and elongation has more than doubled from ~3.4% to ~8% compared with SLMed AlSi10Mg alloy without nano-TiB_2. The strength and ductility

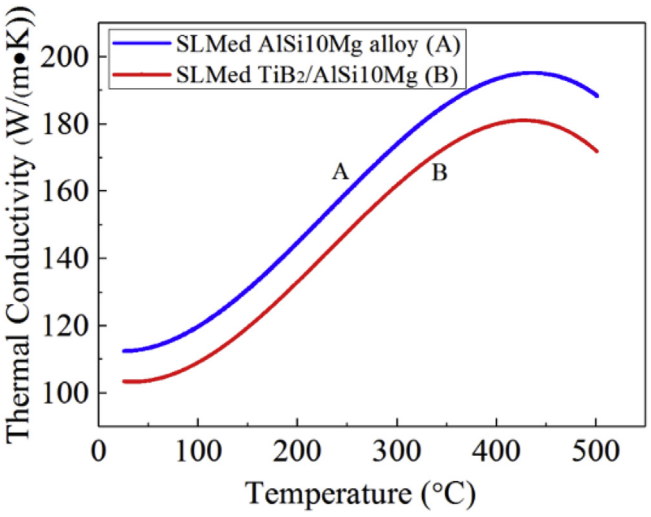

Fig. 11. The thermal conductivity of SLMed AlSi10Mg and TiB_2 decorated AlSi10Mg alloy.

properties have been improved simultaneously in both directions. The strengthening mechanisms have been discussed in the previous study [13], including Orowan strengthening via dispersed nano-TiB_2 particles in the alloy, grain boundary strengthening through the Hall-Petch relation and load-bearing strengthening via strength interfacial bonding between nano-TiB_2 particles and the Al alloy. The mechanisms of strength and ductility concurrent improvement are the same in two directions. Thus, the mechanical anisotropy in SLMed alloy is mitigated.

As mentioned above, the anisotropy of mechanical properties is a key technical problem in metallic alloys produced by SLM. Generally, the presence of strong crystallographic texture in the alloy results in anisotropy in the properties, such as UTS and El. However, the yield strength is mainly related to the inhomogeneous structure in the melt pool boundary but not the texture for SLMed alloy. The similar result was observed and explained by calculating the Schmid factor in different directions [43]. The anisotropy in strength and ductility in the SLMed AlSi10Mg alloy is possibly due to the plastic deformation occurring within the elongated cellular microstructures. The reasonable assumption is that plasticity begins in the α-Al phase. As α-Al cells are surrounded by eutectic Si meshes in the rod-like shape (shown in Fig. 3), plasticity leads to strain localization, debonding and voids nucleation at the α-Al/Si interface. Upon further straining, the coalescence of these voids causes the crack formation and final fracture of the specimen. As the aspect ratio of elongated cellular substructure is up to 4–5. The crack path is more tortuous when the loading direction is parallel to the building direction, which results in higher UTS and El as compared to that when the loading direction is perpendicular to the building direction. Therefore, both properties of strength and ductility along the building direction is better than that perpendicular to the building direction in SLMed alloy. Fractographic analyses of SLMed alloys in different directions shown in Fig. 12 confirm that the fracture occurs predominantly along the coarse, hard Si phase. As illustrated in Fig. 12a, when the sample is loaded perpendicular to the building direction (⊥BD), once the cracks initiate, they will propagate along the hard phases at cell boundaries, inducing the fracture at a lower plasticity. As can be seen in Fig. 12b, when the sample is loaded along building direction (//BD), some small dimples are observed between the cracked hard phases. Thus, the samples exhibit a slightly higher ductility (and also higher strength) in building direction.

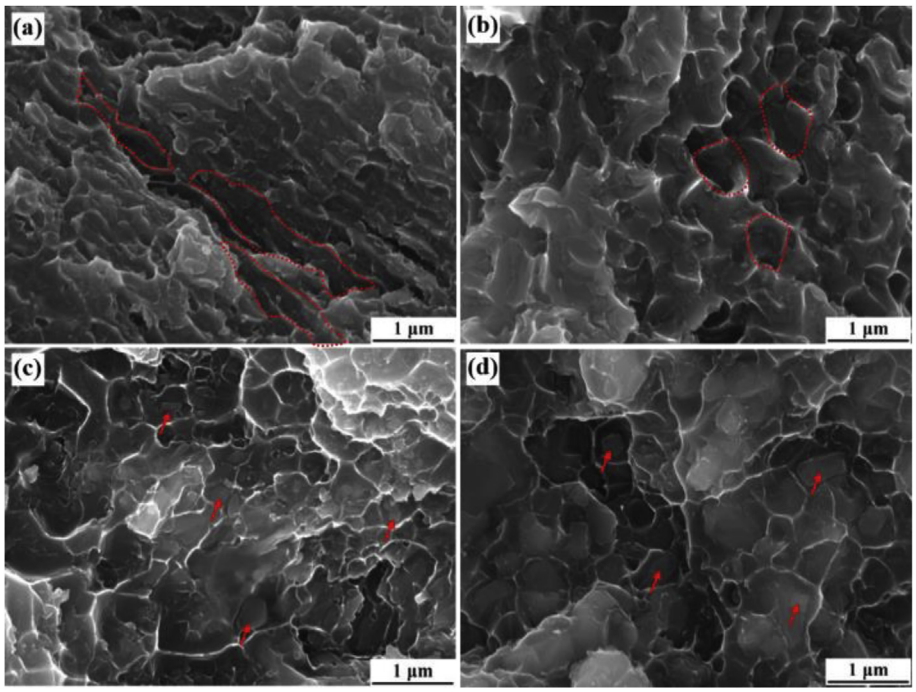

Fig. 12. The SEM fracture surfaces of SLMed AlSi10Mg samples loaded (a) perpendicular to building direction (⊥BD) and (b) along building direction (//BD), and TiB_2 decorated AlSi10Mg samples loaded (c)⊥BD and (d)//BD. The red point circles show the hard Si phases. The red arrows indicate the TiB_2 particles. (For interpretation of the references to colour in this figure legend, the reader is referred to the Web version of this article.)

By contrast, in SLMed TiB_2 decorated AlSi10Mg alloy, the presence of nano-TiB_2 particles influence the microstructures and in turn the mechanical properties. The morphology of the cells and grains change from elongated microstructure to equiaxed substructure with no obvious directionality. As the interface of coarse silicon and Al acts as crack initiation sites, the refinement of eutectic Si phase makes crack initiation more difficult. Even when the cracks initiate, the uniformly distributed nano-TiB_2 particles can deflect the straight growth of cracks. A similar result is revealed in nanoparticles reinforced Al composites after orthogonal thermomechanical processes [44]. It is confirmed by a vast number of fine dimples and intersecting tearing ridges in the fracture surfaces of SLMed samples (Fig. 12c and d). Hence, the cracks expand much slowly and the crack path in different directions is exactly almost the same, leading to isotropic in strength and ductility. Therefore, our result verifies that the anisotropy of SLMed sample is weakened for the existence of *in-situ* nano-TiB_2 particles.

5. Conclusions

This study focuses on *in-situ* TiB_2 nano-particle decorated AlSi10Mg alloy, which is produced by selective laser melting (SLM). The study investigates the microstructure, texture evolution and anisotropic behavior. The main conclusions are summarized as follows:

(1) A competition growth of <100> and <110> fiber texture is found in the SLMed AlSi10Mg alloy. The coarse columnar grains with strong fiber texture dominate the microstructure leading to significant anisotropic properties.
(2) The anisotropic behavior was significantly ameliorated in the SLMed *in-situ* nano-TiB_2 decorated AlSi10Mg alloy. Compared to SLMed AlSi10Mg alloy with coarse columnar grain structure, strong <100> and sub-strong <110> fiber orientation texture, and obvious anisotropy in mechanical properties, the *in-situ* nano-TiB_2 decorated AlSi10Mg alloy exhibits equiaxed grains, no preferred crystallographic texture and reduces the anisotropy remarkably.
(3) The addition of nano-TiB_2 particles leads to columnar-to-equiaxed transition and distinct grain refinement. One reason is the pinning effect of nano-structured particles influencing the heat transfer so that to reduce the gradient of temperature distribution. Another reason is that the particles act as active heterogeneous nucleant substrates to promote nucleant process and the growth inhibitor to restrict the growth of grains.
(4) The strength and ductility have been dramatically improved at the same time in the SLMed *in-situ* nano-TiB_2 alloy. The improvement of properties is mainly due to the significantly fine equiaxed grains in the SLMed AlSi10Mg samples for the presence of uniformly distributed nano-TiB_2 particles.

Conflicts of interest

The authors declare that they have no conflict of interest.

Acknowledgments

This work is financially supported by the National Key Research and Development Program of China (Grant No. 2016YFB1100100). We would like to thank the laboratory CARR, Institute of Atomic Energy, Beijing, China for its help with neutron diffraction experiments and Han Chen at Shanghai Jiao Tong University (China) for his help and fruitful discussions.

References

[1] E. Louvis, P. Fox, C.J. Sutcliffe, Selective laser melting of aluminium components, J. Mater. Process. Technol. 211 (2011) 275–284, https://doi.org/10.3109/14397595.2014.998361.

[2] E.O. Olakanmi, R.F. Cochrane, K.W. Dalgarno, A review on selective laser sintering/melting (SLS/SLM) of aluminium alloy powders: processing, microstructure, and properties, Prog. Mater. Sci. 74 (2015) 401–477, https://doi.org/10.1016/j.pmatsci.2015.03.002.
[3] D. Herzog, V. Seyda, E. Wycisk, C. Emmelmann, Additive manufacturing of metals, Acta Mater. 117 (2016) 371–392, https://doi.org/10.1016/j.actamat.2016.07.019.
[4] X.P. Li, X.J. Wang, M. Saunders, A. Suvorova, L.C. Zhang, Y.J. Liu, M.H. Fang, Z.H. Huang, T.B. Sercombe, A selective laser melting and solution heat treatment refined Al–12Si alloy with a controllable ultrafine eutectic microstructure and 25% tensile ductility, Acta Mater. 95 (2015) 74–82, https://doi.org/10.1016/j.actamat.2015.05.017.
[5] T. Niendorf, S. Leuders, A. Riemer, H.A. Richard, T. Tröster, D. Schwarze, Highly anisotropic steel processed by selective laser melting, Metall. Mater. Trans. B 44 (2013) 794–796, https://doi.org/10.1007/s11663-013-9875-z.
[6] M. Simonelli, Y.Y. Tse, C. Tuck, Effect of the build orientation on the mechanical properties and fracture modes of SLM Ti–6Al–4V, Mater. Sci. Eng. A 616 (2014) 1–11, https://doi.org/10.1016/j.msea.2014.07.086.
[7] B. Song, S. Dong, P. Coddet, H. Liao, C. Coddet, Fabrication of NiCr alloy parts by selective laser melting: columnar microstructure and anisotropic mechanical behavior, Mater. Des. 53 (2014) 1–7, https://doi.org/10.1016/j.matdes.2013.07.010.
[8] L. Thijs, M.L. Montero Sistiaga, R. Wauthle, Q. Xie, J.P. Kruth, J. Van Humbeeck, Strong morphological and crystallographic texture and resulting yield strength anisotropy in selective laser melted tantalum, Acta Mater. 61 (2013) 4657–4668, https://doi.org/10.1016/j.actamat.2013.04.036.
[9] H.L. Wei, J. Mazumder, T. DebRoy, Evolution of solidification texture during additive manufacturing, Sci. Rep. (2015) 1–7, https://doi.org/10.1038/srep16446.
[10] K.G. Prashanth, S. Scudino, J. Eckert, Defining the tensile properties of Al-12Si parts produced by selective laser melting, Acta Mater. 126 (2017) 25–35, https://doi.org/10.1016/j.actamat.2016.12.044.
[11] Z. Fan, Y. Wang, Y. Zhang, T. Qin, X.R. Zhou, G.E. Thompson, T. Pennycook, T. Hashimoto, Grain refining mechanism in the Al/Al–Ti–B system, Acta Mater. 84 (2015) 292–304, https://doi.org/10.1016/j.actamat.2014.10.055.
[12] P.L. Schaffer, D.N. Miller, A.K. Dahle, Crystallography of engulfed and pushed TiB2 particles in aluminium, Scripta Mater. 57 (2007) 1129–1132, https://doi.org/10.1109/TCST.2011.2152842.
[13] X.P. Li, G. Ji, Z. Chen, A. Addad, Y. Wu, H.W. Wang, J. Vleugels, J. Van Humbeeck, J.P. Kruth, Selective laser melting of nano-TiB2decorated AlSi10Mg alloy with high fracture strength and ductility, Acta Mater. 129 (2017) 183–193, https://doi.org/10.1016/j.actamat.2017.02.062.
[14] M. Chen, X. Li, G. Ji, Y. Wu, Z. Chen, W. Baekelant, K. Vanmeensel, H. Wang, J.-P. Kruth, Novel composite powders with uniform TiB2 nano-particle distribution for 3D printing, Appl. Sci. 7 (2017) 250, https://doi.org/10.3390/app7030250.
[15] P. Wang, C. Gammer, F. Brenne, T. Niendorf, J. Eckert, S. Scudino, A heat treatable TiB2/Al-3.5Cu-1.5Mg-1Si composite fabricated by selective laser melting: microstructure, heat treatment and mechanical properties, Compos. B Eng. 147 (2018) 162–168, https://doi.org/10.1016/j.compositesb.2018.04.026.
[16] L.X. Xi, H. Zhang, P. Wang, H.C. Li, K.G. Prashanth, K.J. Lin, I. Kaban, D.D. Gu, Comparative investigation of microstructure, mechanical properties and strengthening mechanisms of Al-12Si/TiB2 fabricated by selective laser melting and hot pressing, Ceram. Int. 44 (2018) 17635–17642, https://doi.org/10.1016/j.ceramint.2018.06.225.
[17] A.B. Spierings, K. Dawson, M. Voegtlin, F. Palm, P.J. Uggowitzer, Microstructure and mechanical properties of as-processed scandium-modified aluminium using selective laser melting, CIRP Ann. - Manuf. Technol. 65 (2016) 213–216, https://doi.org/10.1016/j.cirp.2016.04.057.
[18] A.B. Spierings, K. Dawson, T. Heeling, P.J. Uggowitzer, R. Schäublin, F. Palm, K. Wegener, Microstructural features of Sc- and Zr-modified Al-Mg alloys processed by selective laser melting, Mater. Des. 115 (2017) 52–63, https://doi.org/10.1016/j.matdes.2016.11.040.
[19] R. Li, M. Wang, T. Yuan, B. Song, C. Chen, K. Zhou, P. Cao, Selective laser melting of a novel Sc and Zr modified Al-6.2 Mg alloy: processing, microstructure, and properties, Powder Technol. 319 (2017) 117–128, https://doi.org/10.1016/j.powtec.2017.06.050.
[20] K.V. Yang, Y. Shi, F. Palm, X. Wu, P. Rometsch, Columnar to equiaxed transition in Al-Mg(-Sc)-Zr alloys produced by selective laser melting, Scripta Mater. 145 (2018) 113–117, https://doi.org/10.1016/j.scriptamat.2017.10.021.
[21] H. Attar, M. Bönisch, M. Calin, L.C. Zhang, S. Scudino, J. Eckert, Selective laser melting of in situ titanium-titanium boride composites: processing, microstructure and mechanical properties, Acta Mater. 76 (2014) 13–22, https://doi.org/10.1016/j.actamat.2014.05.022.
[22] C. Cai, B. Song, C. Qiu, L. Li, P. Xue, Q. Wei, J. Zhou, H. Nan, H. Chen, Y. Shi, Hot isostatic pressing of in-situ TiB/Ti-6Al-4V composites with novel reinforcement architecture, enhanced hardness and elevated tribological properties, J. Alloys Compd. 710 (2017) 364–374, https://doi.org/10.1016/j.jallcom.2017.03.160.
[23] J.H. Martin, B.D. Yahata, J.M. Hundley, J.A. Mayer, T.A. Schaedler, T.M. Pollock, 3D printing of high-strength aluminium alloys, Nature 549 (2017) 365–369, https://doi.org/10.1038/nature23894.
[24] Z. Chen, G.A. Sun, Y. Wu, M.H. Mathon, A. Borbely, D. Chen, G. Ji, M.L. Wang, S.Y. Zhong, H.W. Wang, Multi-scale study of microstructure evolution in hot extruded nano-sized TiB 2 particle reinforced aluminum composites, Mater. Des. 116 (2017) 577–590, https://doi.org/10.1016/j.matdes.2016.12.070.
[25] Y. Tang, Z. Chen, A. Borbély, G. Ji, S.Y. Zhong, D. Schryvers, V. Ji, H.W. Wang, Quantitative study of particle size distribution in an in-situ grown Al–TiB2 composite by synchrotron X-ray diffraction and electron microscopy, Mater. Char. 102 (2015) 131–136, https://doi.org/10.1016/j.matchar.2015.03.003.
[26] J. Wu, X.Q. Wang, W. Wang, M.M. Attallah, M.H. Loretto, Microstructure and strength of selectively laser melted AlSi10Mg, Acta Mater. 117 (2016) 311–320, https://doi.org/10.1016/j.actamat.2016.07.012.
[27] L. Thijs, K. Kempen, J.-P. Kruth, J. Van Humbeeck, Fine-structured aluminium products with controllable texture by selective laser melting of pre-alloyed AlSi10Mg powder, Acta Mater. 61 (2013) 1809–1819, https://doi.org/10.1016/j.actamat.2012.11.052.
[28] J. Suryawanshi, K.G. Prashanth, S. Scudino, J. Eckert, O. Prakash, U. Rammamurty, Simultaneous enhancements of strength and toughness in an Al-12Si alloy synthesized using selective laser melting, Acta Mater. 115 (2016) 285–294, https://doi.org/10.1016/j.actamat.2016.06.009.
[29] R. Acharya, J.A. Sharon, A. Staroselsky, Prediction of microstructure in laser powder bed fusion process, Acta Mater. 124 (2017) 360–371, https://doi.org/10.1016/j.actamat.2016.11.018.
[30] K.G. Prashanth, S. Scudino, H.J. Klauss, K.B. Surreddi, L. Löber, Z. Wang, A.K. Chaubey, U. Kühn, J. Eckert, Microstructure and mechanical properties of Al–12Si produced by selective laser melting: effect of heat treatment, Mater. Sci. Eng. A 590 (2014) 153–160, https://doi.org/10.1016/j.msea.2013.10.023.
[31] P. Wang, H.C. Li, K.G. Prashanth, J. Eckert, S. Scudino, Selective laser melting of Al-Zn-Mg-Cu: heat treatment, microstructure and mechanical properties, J. Alloys Compd. 707 (2017) 287–290, https://doi.org/10.1016/j.jallcom.2016.11.210.
[32] U.F. Kocks, C.N. Tome, H.R. Wenk, Texture and Anisotropy, second, Cambrige University Press, Cambrige, 1998.
[33] B. Chen, S.K. Moon, X. Yao, G. Bi, J. Shen, J. Umeda, K. Kondoh, Strength and strain hardening of a selective laser melted AlSi10Mg alloy, Scripta Mater. 141 (2017) 45–49, https://doi.org/10.1016/j.scriptamat.2017.07.025.
[34] X. Ding, L. Wang, Heat transfer and fluid flow of molten pool during selective laser melting of AlSi10Mg powder: simulation and experiment, J. Manuf. Process. 26 (2017) 280–289, https://doi.org/10.1016/j.jmapro.2017.02.009.
[35] J.R. Croteau, S. Griffiths, M.D. Rossell, C. Leinenbach, C. Kenel, V. Jansen, D.N. Seidman, D.C. Dunand, N.Q. Vo, Microstructure and mechanical properties of Al-Mg-Zr alloys processed by selective laser melting, Acta Mater. 153 (2018) 35–44, https://doi.org/10.1016/j.actamat.2018.04.053.
[36] S. Henry, P. Jarry, M. Rappaz, <110> dendrite growth in aluminum feathery grains, Metall. Mater. Trans. A Phys. Metall. Mater. Sci. 29 (1998) 2807–2817, https://doi.org/10.1007/s11661-998-0321-9.
[37] S. Henry, T. Minghetti, M. Rappaz, Dendrite growth morphologies in aluminium alloys, Acta Mater. 46 (1998) 6431–6443, https://doi.org/10.1016/S1359-6454(98)00308-5.
[38] T. Haxhimali, A. Karma, F. Gonzales, M. Rappaz, Orientation selection in dendritic evolution, Nat. Mater. 5 (2006) 660–664, https://doi.org/10.1038/nmat1693.
[39] D.A. Porter, K.E. Easterling, M. Sherif, Phase Transformations in Metals and Alloys, third ed., CRC Press, Talor & Francis Group, 1992.
[40] Y. Li, D. Gu, Parametric analysis of thermal behavior during selective laser melting additive manufacturing of aluminum alloy powder, Mater. Des. 63 (2014) 856–867, https://doi.org/10.1016/j.matdes.2014.07.006.
[41] L. Thijs, F. Verhaeghe, T. Craeghs, J. Van Humbeeck, J. Kruth, A study of the microstructural evolution during selective laser melting of Ti − 6Al − 4V, Acta Mater. 58 (2010) 3303–3312, https://doi.org/10.1016/j.actamat.2010.02.004.
[42] P. Yuan, D. Gu, Molten pool behaviour and its physical mechanism during selective laser melting of TiC/AlSi10Mg nanocomposites : simulation and experiments, J. Phys. D Appl. Phys. (2015), 035303, https://doi.org/10.1088/0022-3727/48/3/035303, 35303.
[43] Z.H. Xiong, S.L. Liu, S.F. Li, Y. Shi, Y.F. Yang, R.D.K. Misra, Role of melt pool boundary condition in determining the mechanical properties of selective laser melting AlSi10Mg alloy, Mater. Sci. Eng. A 741 (2019) 148–156, https://doi.org/10.1016/j.msea.2018.10.083.
[44] J. Liu, Z. Chen, F. Zhang, G. Ji, Y. Ma, M. Wang, S. Zhong, J. Li, H. Wang, H. Wang, Improved structural homogeneity and mechanical properties of nanoparticles reinforced Al composites after orthogonal thermomechanical processes, J. Alloys Compd. 767 (2018) 293–301, https://doi.org/10.1016/j.jallcom.2018.07.083.